

# A flexible solution for seepage problems integrating SBFEM and recursive polytree meshing

Guoyang Yi<sup>a,b</sup>, Degao Zou<sup>a,b,\*</sup>, Kai Chen<sup>a,b,\*</sup>, Mingliang Zhang<sup>a,b</sup>, Shaoyun Pang<sup>a,b</sup>

<sup>a</sup> The State Key Laboratory of Coastal and Offshore Engineering, Dalian University of Technology, Dalian, Liaoning 116024, China

<sup>b</sup> School of Infrastructure Engineering, Dalian University of Technology, Dalian, Liaoning 116024, China

## ARTICLE INFO

### Keywords:

SBFEM  
Cross-scale  
Seepage  
Adaptive analysis  
Earth-rock dam

## ABSTRACT

In this paper, a flexible analysis method for the seepage problem is proposed by improving the traditional scaled boundary finite element method (SBFEM) and automatically adapting the polytree-based refinement algorithms. Firstly, by embedding integration points inside the boundary element instead of the traditional boundary integration scheme, the dynamic evolution process of the free water surface inside the cell can be directly described, which overcomes the limitations of the traditional boundary integration method. Subsequently, the innovative integration of SBFEM into a static grid iterative framework avoids the problem of frequent re-meshing of conventional SBFEM due to free water surface motion. In order to take full advantage of the cross-scale meshing of SBFEM, adaptive refinement based on a polytree algorithm and a free surface position indicator is implemented, and the accuracy is dynamically controlled by error feedback. Then, the above algorithm is integrated into the finite element software GEODYNA based on object-oriented programming architecture. Finally, the correctness and effectiveness of the proposed method are verified by carrying out seepage analysis on the earth-rock dam. The results show that the proposed method can perform cross-scale analyses in critical regions, thus effectively improving the computational efficiency without affecting the solution accuracy.

## 1. Introduction

Modeling infiltration flow in soils is a fundamental challenge that involves multiple disciplinary areas, including agricultural sciences, geoenvironment and energy recovery processes. Accurate modeling of infiltration flows not only contributes to the understanding of water movement in soils, but also provides important data to support resource management and environmental protection. In the study of seepage phenomena, researchers have proposed a variety of theories and methods, including analytical [1,2], graphical [3] and numerical methods. The analytical method relies on precise mathematical expressions to describe physical processes, but its application is limited when faced with practical situations such as complex boundary conditions and non-homogeneous media. And the graphical method relies on the experience and skill of the mapper to improve the accuracy, but this also limits its scope of application and precision. In view of the limitations of the above two methods, researchers are more likely to use numerical methods to explore and analyze seepage problems.

The finite volume method (FVM) is a common method for solving infiltration flow problems, and its core idea is to integrate the equations

over a control body to ensure the conservation of physical quantities such as mass and momentum. The method has been widely used in modeling infiltration flow [4–7], and it is especially good in soil moisture transport simulations where water conservation needs to be strictly satisfied. However, FVM is relatively cumbersome in dealing with complex boundary conditions. The finite difference method (FDM) is also one of the commonly used methods for solving seepage problems, but its discrete approach based on structured grids has limitations in simulating complex geometries, and the accuracy needs to be improved by optimizing the difference format or locally encrypting the mesh [8–11]. In contrast, the finite element method (FEM) is naturally applicable to unstructured grids and can handle complex boundaries and irregular regions more flexibly [12–15], and thus has wider applicability in seepage problems.

With the continuous proposal of new and efficient algorithms, numerical analysis methods are moving towards higher accuracy, aiming at obtaining the distribution of physical fields more accurately. For example, Jiang et al. [16] used a dynamic contact algorithm to assess the seismic performance of gravity dams. Chen et al. [17] used an incremental dynamic analysis algorithm to investigate the potential damage

\* Corresponding authors.

E-mail addresses: [zoudegao@dlut.edu.cn](mailto:zoudegao@dlut.edu.cn) (D. Zou), [chenkai@dlut.edu.cn](mailto:chenkai@dlut.edu.cn) (K. Chen).

<https://doi.org/10.1016/j.enganabound.2025.106389>

Received 7 May 2025; Received in revised form 3 July 2025; Accepted 3 July 2025

Available online 10 July 2025

0955-7997/© 2025 Elsevier Ltd. All rights are reserved, including those for text and data mining, AI training, and similar technologies.

modes of concrete dams under seismic loading. Xu et al. [18] proposed an improved seepage detection algorithm based on the pseudo-flow field method, which provides an effective means for the rapid and accurate identification of dam seepage hazards by optimizing the measurement line arrangement and numerical simulation analysis. Wang et al. [19] proposed a landslide surge probability analysis method based on the energy equivalence method, physical model experiment and machine learning agent model, which provides a novel approach for risk assessment, prevention and control of landslide surge disaster chain in mountain reservoirs. Chen et al. [20] innovatively combined the inverse modeling analysis method of artificial neural network and genetic algorithm to reveal the exponential decay of bedrock permeability of high arch dams with operation time. Yang et al. [21,22] used a cross-scale algorithm to solve the viscoelasticity problem of non-homogeneous materials. Among them, the cross-scale algorithm, as a high-performance computational method, is able to achieve a satisfactory balance between solution accuracy and computational efficiency. The main idea of this algorithm is to arrange fine-scale grids in critical areas of the structure to capture local details, while using coarse-scale grids in other areas to improve computational efficiency. Between the fine-scale and coarse-scale meshes, a transition mesh (generally a polygonal mesh) is used to smoothly connect these two different scales. However, the traditional FEM cannot solve for polygonal cells, so it needs to be combined with other advanced numerical methods to realize coarse-scale analysis.

Recently, Wolf and Song [23] proposed a semi-analytical SBFEM, which provides an effective alternative for cross-scale refinement analysis due to the advantage of easy construction of polygonal or polyhedral cells. In recent years, after the systematic research of Song [24–27], the theoretical system of SBFEM has matured and has been widely applied in many fields. For example, Zhao et al. [28–30] created the Scaled Boundary Perfect Matching Layer (SBPML) by applying the local coordinate system of SBFEM to the artificial boundary method to achieve lossless coupling of complex geometric boundaries, providing an effective approach for engineering applications. Zhang et al. [31,32] constructed an explicit parallel computation system based on the SBFEM, which achieves efficient discretisation of the computational domain and accurate transfer of dynamic loads by introducing the octree adaptive mesh technique, and solves the time-step limitation of the traditional implicit algorithms in wave propagation problems. Liu et al. [33,34] realized the accurate transformation of 3D thin-walled structures to 2D computational models based on the theory of dimensionality reduction modelling of SBFEM through the synergistic mechanism of boundary discretization and analytical solving in the direction of the thickness, which effectively overcame the problem of accuracy loss due to the mesh locking effect of the traditional finite element method in the analysis of thin-walled structures. Benefiting from the advantage that SBFEM can handle arbitrary polygons, Du et al. [35–37] created a crack extension solution method, which provides engineers with an efficient and high-precision fracture simulation solution. Ooi et al. [38–40] effectively solves the numerical challenges in elastic mechanics and crack extension simulation of functionally gradient materials based on SBFEM and by introducing higher-order bubble functions and polygonal cells, which significantly improves the computational accuracy, efficiency, and convergence of the stress field and fracture parameters. In the research and development of nonlinear analysis algorithms, Chen et al. [41,42] developed an efficient and practical polygonal and polyhedral SBFEM elastic-plastic analysis algorithm, which breaks through the technical constraints of elasticity analysis that SBFEM has been limited to for a long time. In order to balance the inherent contradiction between accuracy and efficiency in numerical simulation, Zou et al. [43,44] successfully developed cross-order SBFEM, a method that supports multiple cell shapes and variable computational orders, providing both high accuracy for complex engineering problems. Zhuo et al. [45] coupled the SBFEM with the fracture phase field model, established a mixed-mode fracture analysis framework applicable to rock-like

materials, and successfully realized the simulation of the whole process of crack extension under tensile-compressive-shear composite loading.

With the gradual maturity of SBFEM theory, its application research in the field of fluids also shows rapid development. For example, Zou et al. [46,47] proposed SBFEM for nonlinear dynamic analysis of saturated porous media based on generalized Biot's dynamic consolidation theory. Mohammad [48,49] proposed SBFEM for solving steady state seepage and transient seepage problems. Liu [50] proposed an isogeometric SBFEM and applied it to the seepage analysis of dams on infinite foundations. Yang [51,52] implemented the PSBEM algorithm in the framework of the user subroutine (UEL) of the finite element software ABAQUS and applied it to the transient seepage analysis of an earth and rock dam. In addition, studies have also reported the application of SBFEM in the field of stochastic [53] and singular [54] seepage.

However, as reported in the above literature [48–50], researchers are combining SBFEM with a moving grid system to determine the location of the free water surface of an earth and rock dam, a strategy that has limitations. Specifically, this type of method requires constant adjustment of node positions during the iteration process, which may lead to distortions of the cells, making it difficult to apply to complex models (complex geometries or sudden changes in permeability coefficients of materials).

On the other hand, the position error of the free water surface is also affected by the grid optimization strategy. Since the free surface boundary of the seepage field cannot be determined in advance, the final head distribution needs to be approximated step by step by an iterative method, which introduces a boundary nonlinearity problem. Therefore, it is necessary to refine the grid near the free water surface to reduce the error generated by the iterative process. In addition, what size of grid to be arranged is also a problem worth exploring.

In order to accurately determine the location of the free water surface of the earth-rock dam, this study innovatively combines the SBFEM with a static grid system, and proposes a novel coupled iterative algorithm to avoid frequent re-demarcation of the grid. Firstly, the integration point is introduced inside the boundary cell, which overcomes the difficulty of the traditional SBFEM to consider the free water surface changes inside the cell due to its semi-analytical characteristics. Then, by discounting the permeability coefficients of the Gaussian points inside the cell in the negative pressure zone, the position of the free water surface can be corrected. By developing an adaptive criterion based on a posteriori error estimation, the cells through which the free water surface passes are refined at multiple levels in order to gradually reduce the error due to the unrefined mesh during the iterative process. Finally, the above algorithm is integrated into the finite element software GEO-DYNA, and the accuracy of the method is verified by arithmetic examples for different problems.

The paper is organized as follows: The adaptive SBFEM for the seepage problem of earth and rock dams, including its theoretical framework and the specific steps of adaptive analysis, is described in Section 2. The development platform of the proposed method is introduced in Section 3. The correctness and effectiveness of the proposed method are verified through several numerical examples in Section 4. Finally, the work is concluded in Section 5.

## 2. Adaptive SBFEM for seepage problems

### 2.1. Implementation of the SBFEM

#### 2.1.1. Coordinate transformation

In the polygonal cell shown in Fig. 1, a  $(\xi, \eta)$  local coordinate system is defined with the form centre of the cell as the coordinate origin. The coordinate origin is the scale centre. The line connecting the two endpoints of the line cell and the centre of proportionality forms a subdomain. In each subdomain,  $\xi$  takes the value 0 at the centre of proportionality  $O$  and 1 at the boundary, and  $\eta$  takes the values  $+1, -1$  at the two endpoints of the line cell. By introducing the interpolation

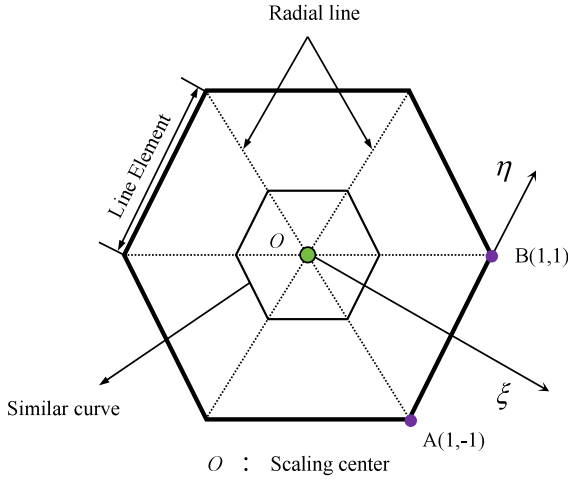


**Fig. 1.** Polygonal representation of a finite element with proportional boundary.

function  $N(\eta)$ , the coordinates of any point on the linear cell can be expressed in the form of Eqs. (2.1) and (2.2). In this study, a two-node linear cell is used, so the expression is Eq. (2.3).

$$x_\eta(\eta) = [N(\eta)]\{x\} \quad (2.1)$$

$$y_\eta(\eta) = [N(\eta)]\{y\} \quad (2.2)$$

$$N(\eta) = [(1-\eta)/2, (1+\eta)/2] \quad (2.3)$$

In Eqs. (2.1) and (2.2),  $\{x\}$  and  $\{y\}$  are the coordinate vectors of the two endpoints of the line unit, respectively.

By this way of definition, the coordinates of any point in the subdomain can be obtained by scaling to the centre of proportionality, the specific expressions of which are shown in Eqs. (2.4) and (2.5).

$$x(\xi, \eta) = \xi[N(\eta)]\{x\} \quad (2.4)$$

$$y(\xi, \eta) = \xi[N(\eta)]\{y\} \quad (2.5)$$

### 2.2.2. Steady-state seepage equation and its solution

The basic governing equation for steady state seepage in two dimensions is:

$$k_x \frac{\partial^2 h}{\partial x^2} + k_y \frac{\partial^2 h}{\partial y^2} = 0 \quad (2.6)$$

Here,  $k_x$  and  $k_y$  denote the permeability coefficients in the direction of the two axes in the Cartesian coordinate system.

Within the proportional boundary coordinate system, the head at any point within the interior of the subdomain can be obtained by interpolation.

$$h(\xi, \eta) = [N_p(\eta)]\{h(\xi)\} \quad (2.7)$$

Here the nodal head function  $\{h(\xi)\}$  is introduced, which represents the head along a radial line.  $[N_p(\eta)]$  is the shape function of a polygonal cell with the following expression:

$$[N_p(\eta)] = [N_1(\eta), N_2(\eta), \dots, N_n(\eta)] \quad (2.8)$$

And the differential operator in the Cartesian coordinate system can also be converted to a differential operator in the local coordinate system by the following equation.

$$\left\{ \begin{array}{l} \frac{\partial}{\partial x} \\ \frac{\partial}{\partial y} \end{array} \right\} = \{b^1(\eta)\} \frac{\partial}{\partial \xi} + \frac{1}{\xi} \{b^2(\eta)\} \frac{\partial}{\partial \eta} \quad (2.9)$$

$$\{b^1(\eta)\} = \frac{1}{|J(\eta)|} \left\{ \begin{array}{l} y_\eta(\eta)_{,\eta} \\ -x_\eta(\eta)_{,\eta} \end{array} \right\} \quad (2.10)$$

$$\{b^2(\eta)\} = \frac{1}{|J(\eta)|} \left\{ \begin{array}{l} -y_\eta(\eta) \\ x_\eta(\eta) \end{array} \right\} \quad (2.11)$$

$$|J(\eta)| = y_\eta(\eta)_{,\eta} x_\eta(\eta) - y_\eta(\eta) x_\eta(\eta)_{,\eta} \quad (2.12)$$

Substituting Eq. (2.7) into Eq. (2.9) will produce the following result:

$$\left\{ \begin{array}{l} \frac{\partial h}{\partial x} \\ \frac{\partial h}{\partial y} \end{array} \right\} = \{B^1(\eta)\} \{h(\xi)\}_{,\xi} + \frac{1}{\xi} \{B^2(\eta)\} \{h(\xi)\} \quad (2.13)$$

Where:

$$\{B^1(\eta)\} = \{b^1(\eta)\} [N(\eta)] \quad (2.14)$$

$$\{B^2(\eta)\} = \{b^2(\eta)\} [N(\eta)]_{,\eta} \quad (2.15)$$

By using the principle of virtual work, the proportional boundary finite element governing equations for steady state seepage can be obtained.

$$[E^0] \xi^2 \{h(\xi)\}_{,\xi\xi} + ([E^0] - [E^1] + [E^1]^T) \xi \{h(\xi)\}_{,\xi} - [E^2] \{h(\xi)\} = 0 \quad (2.16)$$

where  $[E^0]$ ,  $[E^1]$ , and  $[E^2]$  are the matrices associated with the material:

$$[E^0] = \int_S [B^1(\eta)]^T [k] [B^1(\eta)] |J(\eta)| d\eta \quad (2.17)$$

$$[E^1] = \int_S [B^1(\eta)]^T [k] [B^1(\eta)] |J(\eta)| d\eta \quad (2.18)$$

$$[E^2] = \int_S [B^1(\eta)]^T [k] [B^1(\eta)] |J(\eta)| d\eta \quad (2.19)$$

$$[k] = \begin{bmatrix} k_x & \\ & k_y \end{bmatrix} \quad (2.20)$$

Eq. (2.16) is a second order Euler-Cauchy equation which can be transformed into a first order ordinary differential equation shown in Eq. (2.21) by substitution of variables

$$\xi \left\{ \begin{array}{l} \{h(\xi)\} \\ \{q(\xi)\} \end{array} \right\}_{,\xi} = -[Z] \left\{ \begin{array}{l} \{h(\xi)\} \\ \{q(\xi)\} \end{array} \right\} \quad (2.21)$$

Where:

$$[Z] = \begin{bmatrix} [E^0]^{-1} [E^1]^T & -[E^0]^{-1} \\ -[E^2] + [E^1] [E^0]^{-1} [E^1]^T & -[E^1] [E^0]^{-1} \end{bmatrix} \quad (2.22)$$

Therefore, the solution of Eq. (2.16) can be obtained by calculating the eigenvalues and eigenvectors of  $[Z]$

$$[Z] \begin{bmatrix} [\psi_{11}] & [\psi_{12}] \\ [\psi_{21}] & [\psi_{22}] \end{bmatrix} = \begin{bmatrix} [\psi_{11}] & [\psi_{12}] \\ [\psi_{21}] & [\psi_{22}] \end{bmatrix} \begin{bmatrix} [\lambda_p] & \\ & [\lambda_q] \end{bmatrix} \quad (2.23)$$

The matrices  $[\lambda_p]$  and  $[\lambda_q]$  are diagonal arrays consisting of the negative and positive eigenvalues of the matrix  $[Z]$ , respectively. Therefore, the solution of Eq. (2.16) containing the integration constant is as follows:

$$\{h(\xi)\} = [\psi_{11}] \xi^{-[\lambda_p]} \{c_1\} + [\psi_{12}] \xi^{-[\lambda_q]} \{c_2\} \quad (2.24)$$

$$\{q(\xi)\} = [\psi_{21}] \xi^{-[\lambda_p]} \{c_1\} + [\psi_{22}] \xi^{-[\lambda_q]} \{c_2\} \quad (2.25)$$

Notice that the head value at the centre of proportionality has to

satisfy the finiteness condition, when  $\{c_2\}$  must be a zero vector. Under this condition, Eqs. (2.24) and (2.25) will be rewritten as

$$\{h(\xi)\} = [\psi_{11}] \xi^{-[\lambda_p]} \{c_1\} \quad (2.26)$$

$$\{q(\xi)\} = [\psi_{21}] \xi^{-[\lambda_p]} \{c_1\} \quad (2.27)$$

Here the constant of integration  $\{c_1\}$  can be obtained from the nodal head vector  $\{h_b\} = \{h(\xi = 1)\}$  at the boundary.

$$\{c_1\} = \psi_{11}^{-1} \{h_b\} \quad (2.28)$$

Then substituting Eq. (2.26) into Eq. (2.7), and the expression for the head field within the polygonal cell is:

$$h(\xi, \eta) = [N_p(\eta)] [\psi_{11}] \xi^{-[\lambda_p]} [\psi_{11}]^{-1} \{h_b\} \quad (2.29)$$

To improve the generality of the algorithm, Eq. (2.29) can be rewritten in the form of Eq. (2.30). In this way, the SBFEM solution framework is identical to the FEM solution framework.

$$h(\xi, \eta) = [\Phi(\xi, \eta)] \{h_b\} \quad (2.30)$$

Where:

$$[\Phi(\xi, \eta)] = [N_p(\eta)] [\psi_{11}] \xi^{-[\lambda_p]} [\psi_{11}]^{-1} \quad (2.31)$$

Substituting Eq. (2.30) into Eq. (2.13) will produce the following result:

$$\left\{ \begin{array}{c} \frac{\partial h}{\partial x} \\ \frac{\partial h}{\partial y} \end{array} \right\} = [B(\xi, \eta)] \{h_b\} \quad (2.32)$$

$$[B(\xi, \eta)] = [[B^1(\eta)] [\psi_{11}] [-\lambda_p] + B^2(\eta) [\psi_{11}]] \xi^{[-\lambda_p] - [H]} [\psi_{11}]^{-1} \quad (2.33)$$

### 2.2.3. Determination of free water surface

As shown in Fig. 2, driven by the head difference  $h$  formed between the upstream water level and the downstream water level, a free water surface boundary is formed in the dam body, which divides the earth and rock dam into saturated and unsaturated regions. Since the free water surface boundary cannot be determined in advance, the real solution must be approximated step by step through an iterative method.

In 1979, Bathe [55] proposed a cell conductivity matrix adjustment method to determine the location of the free water surface within the finite element solution framework, which locates the free water surface by discounting the permeability coefficients of the cells through which the free water surface passes (transition zone cells) as well as the cells in the unsaturated zone. This subsection extends this method to the SBFEM framework.

In steady state seepage calculations, the expression for the conductance matrix of the cell is given by Eq. (2.34).

$$[K] = \int_{\Omega} [B(\xi, \eta)]^T [k(\xi, \eta)] [B(\xi, \eta)] J(\eta) |d\xi d\eta| \quad (2.34)$$

Since conventional SBFEM discretizes only at the boundary of the cell, it cannot capture the variation of the free water surface inside the cell. Therefore this study captures the position of the free water surface

by introducing internal integration points inside the cell.

Considering that the integral is additive with respect to the region, Eq. (2.34) can be rewritten in the form of Eq. (2.35).

$$[K] = \sum_{i=1}^n \int_{\Omega_i} [B(\xi, \eta)]^T [k(\xi, \eta)] [B(\xi, \eta)] J(\eta) |d\xi d\eta| \quad (2.35)$$

Using the Hammer integral for Eq. (2.35), Eq. (2.34) is eventually written in the form of Eq. (2.36).

$$[K] = \sum_{i=1}^n \sum_{j=1}^m \int_{\Omega_i} [B(\xi_j, \eta_j)]^T [k(\xi_j, \eta_j)] [B(\xi_j, \eta_j)] J(\eta_j) |d\xi_j d\eta_j| \quad (2.36)$$

The whole integration process is shown in Fig. 3 ( $n = 5, m = 3$ ).

In Eq. (36), the value of  $k(\xi_j, \eta_j)$  is related to the pore pressure  $p(\xi_j, \eta_j)$  at that point, and if  $p(\xi_j, \eta_j)$  is less than 0, the value of  $k(\xi_j, \eta_j)$  should be discounted.

The locations and weights of the triangular Hammer integration points are given in Table 1, and the reader can go ahead and select the appropriate integration scheme according to the requirements. In this study, a scheme with 3 integration points is used.

### 2.3. Implementation of adaptive analysis

#### 2.3.1. Grid recursive subdivision algorithm based on the idea of polytree decomposition

It is well known that the quality and fineness of the mesh play an important role in the results of numerical analyses. In general, using a coarse mesh means that satisfactory results will not be obtained, while globally adopting a fine mesh will drastically reduce the computational efficiency. Therefore, in this subsection we explore a mesh refinement algorithm based on the idea of polytree for local refinement.

Inspired by the polytree decomposition technique, the algorithm can be implemented in the following steps. For quadrilateral cells, the quadtree rule is strictly followed for 4 equal subdivisions. For  $n$ -sided cells ( $n$  is greater than 4), it can also be regularly subdivided into  $n$  pentagonal cells with 1  $n$ -sided cell. Taking quadrilateral, pentagon and hexagon as examples, the whole process of unit refinement is shown in Fig. 4.

The most prominent advantage of this algorithm is its ability to accurately refine locally (as shown in Fig. 5). When the algorithm applies local refinement to critical areas near the free water surface, hanging nodes will inevitably be generated in the coarse-fine mesh transition zone. Traditional FEM are usually complicated and cumbersome to deal with such problems. In contrast, the SBFEM adopted in this paper, through its unique scale-centred analytical framework, can directly treat the  $n$ -sided cell containing  $m$  hanging nodes as an  $(m + n)$ -side cell for solving without any additional constraints.

#### 2.4. Steps in adaptive analysis

After the initial calculations have determined the free water surface, the recursive algorithm described in the previous section can be used to refine the cells that pass through the free water surface. By repeating this process over and over again, the position of the free water surface will gradually approach the actual situation. Fig. 6 shows a schematic representation of how the free water surface position changes during the adaptive process.

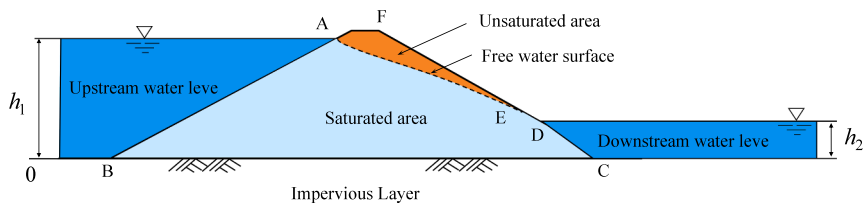


Fig. 2. Schematic of seepage boundaries of an Earth-rock dam.

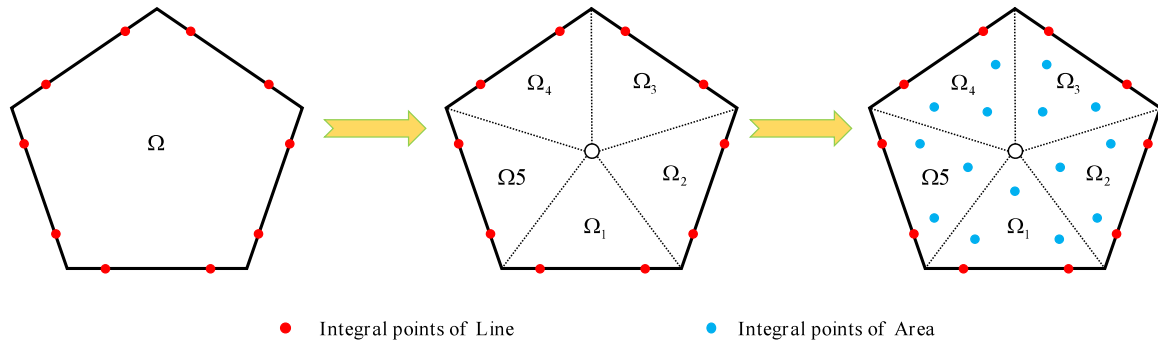
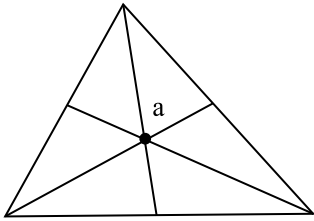
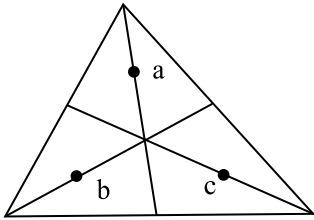
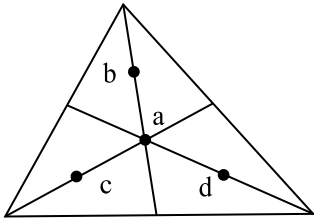


Fig. 3. Schematic diagram of the integration process.

Table 1

Locations and weights of Hammer integration points.

Accuracy	Location	Error	Points	Coordinates	Weight
Liner		$o(h^2)$	$a$	$\frac{1}{3} \frac{1}{3} \frac{1}{3}$	1
Quadratic		$o(h^3)$	$a$ $b$ $c$	$\frac{2}{3} \frac{1}{6} \frac{1}{6}$ $\frac{1}{2} \frac{1}{2} \frac{1}{6}$ $\frac{1}{6} \frac{1}{6} \frac{1}{2}$	$\frac{1}{3}$ $\frac{1}{6}$ $\frac{1}{6}$
Third order		$o(h^4)$	$a$ $b$ $c$ $d$	$\frac{1}{4} \frac{1}{4} \frac{1}{4}$ $\frac{3}{16} \frac{1}{4} \frac{1}{4}$ $\frac{1}{16} \frac{1}{4} \frac{1}{4}$ $\frac{1}{16} \frac{1}{4} \frac{1}{4}$	$\frac{27}{48}$ $\frac{25}{48}$ $\frac{25}{48}$ $\frac{25}{48}$

\* Since the integration domain of the triangle involves the variables themselves, the sum of the weights should be equal to 1/2, so the weights listed in the table should be multiplied by 1/2.

When the amount of free water surface position change obtained from the calculation of two adjacent iterations is close (as shown in Eq. (2.37)), it indicates that the grid has reached the convergence criterion, at which point the adaptive analysis process can be terminated.

$$\|y_{i-1}(x) - y_i(x)\| \leq \varepsilon \quad (2.37)$$

Eq. (2.37) can be used as an a posteriori error estimator for the adaptive analysis, where  $y_{i-1}(x)$  and  $y_i(x)$  denote the function of the free surface position for the last iteration and the current iteration, respectively,  $\varepsilon$  is a given tolerance.

Since the shape of the free water surface usually has nonlinear characteristics, it is difficult to calculate the left end term of Eq. (2.37) accurately by analytical methods, so this paper adopts an approximation method based on sample points. Specifically,  $n-1$  sample points (shown in Fig. 7) are inserted at equal intervals along the free water surface between the water level infiltration point and the overflow point obtained in the previous iteration, and the left end term of Eq. (2.37) is numerically calculated using these sample points. In this way, the

complex nonlinear problem can be simplified effectively.

Thus, the practical form of Eq. (2.37) can be specified as follows:

$$\frac{1}{n} \sum_{j=1}^n |y_{i-1}(x_j) - y_i(x_j)| \leq \varepsilon \quad (2.38)$$

### 3. Development platform

In this study, the proposed adaptive percolation algorithm is deeply integrated into the self-developed finite element software GEODYNA through modern C++ object-oriented programming techniques. The programme employs memory pool optimization techniques and sparse matrix compression storage strategies, resulting in a substantial reduction in memory occupation for problems of the same size.



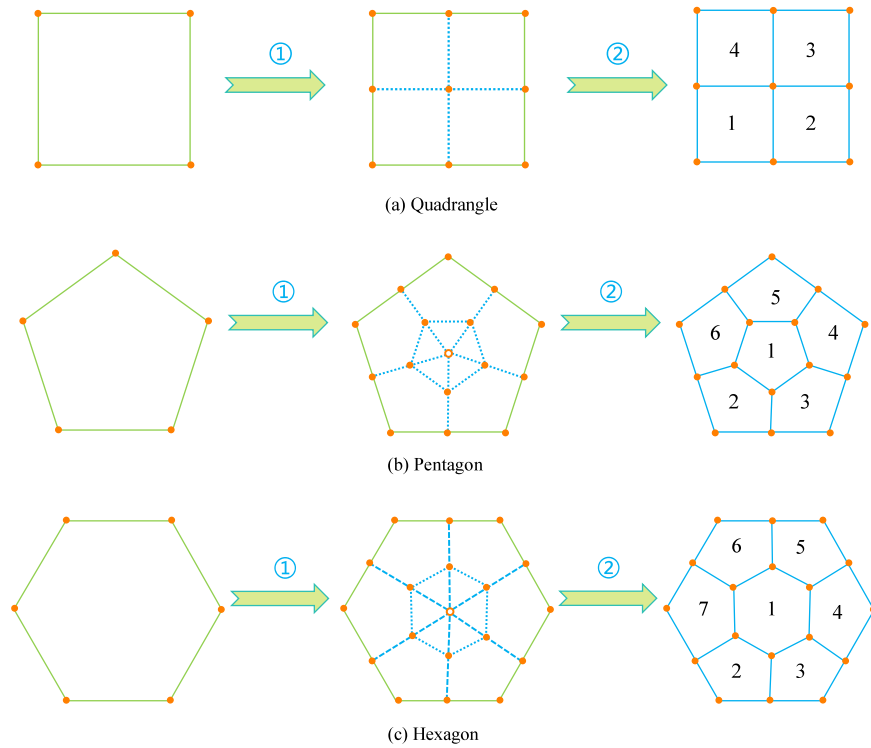


Fig. 4. Element refinement rules.

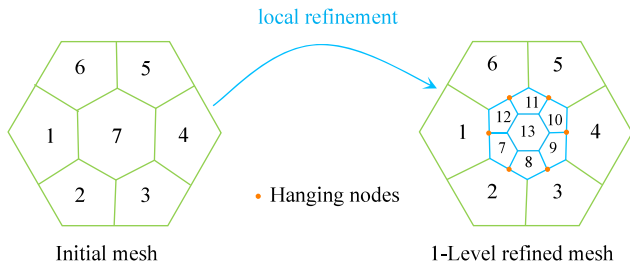


Fig. 5. Schematic representation of the local refinement of the unit.

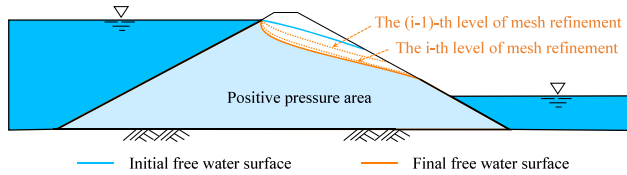


Fig. 6. Schematic representation of free water surface changes during the adaptive process.

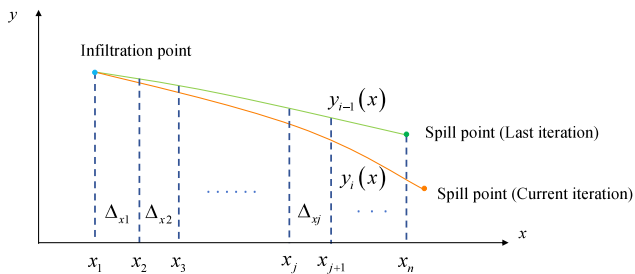


Fig. 7. Sample point selection rule.

## 4. Numerical example

### 4.1. Validation of infiltration flow in a one-vertical earth dam

#### 4.1.1. Geometrical modelling and finite element meshing

A two-dimensional benchmark problem is computed to verify the correctness of the numerical integration. A vertical earth dam with a width of 5 m and a height of 10 m with an upstream water level of 8 m and a downstream water level of 2 m is studied (Fig. 8).

The computational domain is discretized by 51 quadrilateral cells and 231 nodes as shown in Fig. 9. Numerical simulation of the vertical dam is carried out using SBFEM.

In order to verify the correctness of the algorithms in this software, the finite element software GeoStudio software is also used to model the vertical earth dam. The mesh shown in Fig. 9 is also used for this analysis.

#### 4.1.2. Vertical earth dam analysis results

The total head distributions and pressure head distributions of

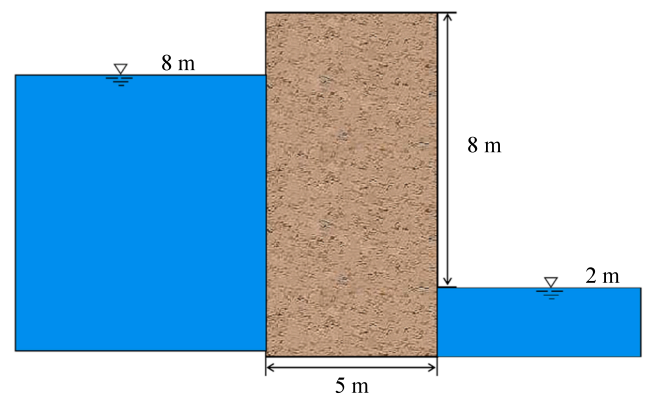


Fig. 8. Two-dimensional vertical earth dam.

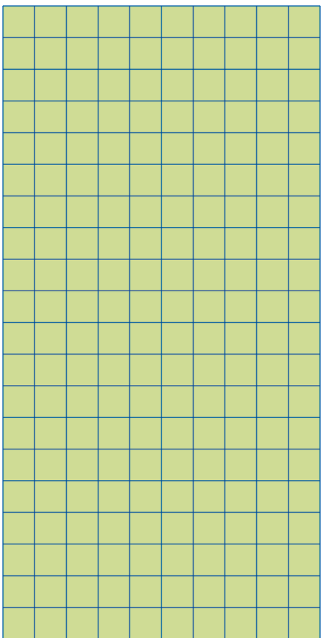


Fig. 9. Typical quadrilateral grid with 200 quadrilateral cells and 231 nodes.

different numerical methods are shown in Figs. 10 and Fig. 11, respectively. From the distributions of the cloud diagrams, it can be seen that the trends of the results calculated by the two procedures are identical. Meanwhile, Table 2 also counts the maximum value of head between different methods. Further analyzed in conjunction with the data in Table 2, the two methods achieved the same results in calculating the maximum and minimum values of total head and pressure head, which also further confirmed the calculation accuracy of SBFEM.

4.2. Adaptive analysis of mean trapezoidal earth dams

4.2.1. Geometric modelling and finite element mesh

The second calculation example is an infiltration flow analysis of a trapezoidal earth dam using an adaptive approach. Fig. 12 illustrates the geometrical model of an earth dam and the elevations of the upstream and downstream water levels, with the infiltration coefficient set to  $10^{-5}$

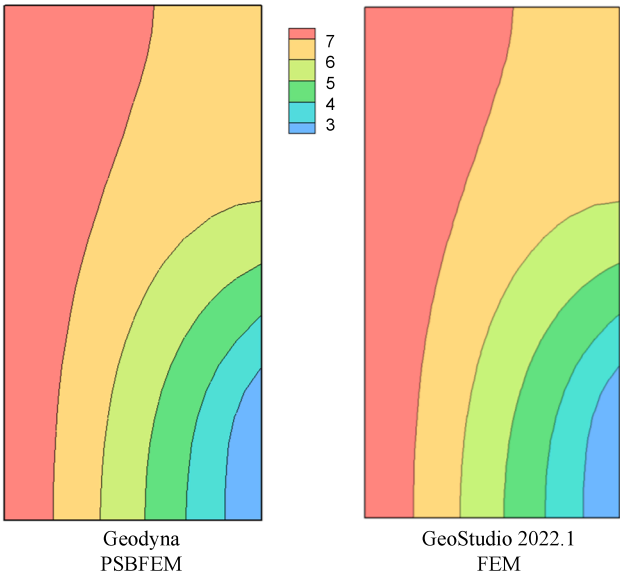


Fig. 10. Vertical earth dam total head distribution (units: m).

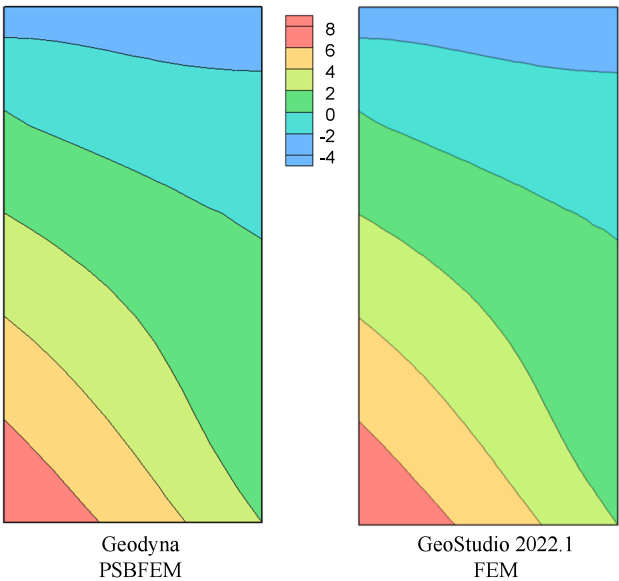


Fig. 11. Vertical earth dam pressure head distribution (units: m).

Table 2  
Statistics of nodal head results.

Variable value (m)	Total head (Max)	Total head (Min)	Pressure head (Max)	Pressure head (Min)
PSBFEM	8.00	2.00	8.00	-3.18
FEM (GeoStudio)	8.00	2.00	8.00	-3.18

m/s.

The polygonal cells shown in Fig. 13 are used to discretize the computational region, generating a total of 87 cells and 175 nodes.

4.2.2. Adaptive analysis process

Fig. 14 gives the position of the infiltration line at the time of the first calculation, which divides the dam into saturated and unsaturated zones. Based on this division, the following three types of elements are defined:

- (1) Saturated elements: it is the element that is completely saturated.
- (2) Transition element: it is the element in the transition region from saturated to unsaturated state. In the adaptive analysis, this cell should be subdivided (as shown in Fig. 15) and the conduction matrix should be calculated according to Eq (2.36).
- (3) Unsaturated element: It is a element in a completely unsaturated state, and the permeability coefficient should be discounted in the calculation.

In order to explore the extent to which the infiltration line changes near the infiltration and overflow points during the adaptive analysis, two observation points, A(244, 135) and B(392, 74) , were placed in these critical areas.

In this algorithm, Eq. (2.38) is used as the criterion for adaptive convergence. Here,  $n$  is taken as 20 and  $\epsilon$  is taken as  $1e-3$ .

4.2.3. Analysis of results for trapezoidal earth dams

Fig. 16 illustrates the finite element mesh used for the adaptive analysis and it can be seen that the mesh has been refined twice. Fig. 17 illustrates the change in the dip line during the adaptive analysis. As can be seen from the figure, there is a head difference of approximately 4.5 m in the dip line when calculated using the initial mesh (compared to the results after the second adaptive analyses). This is mainly due to the

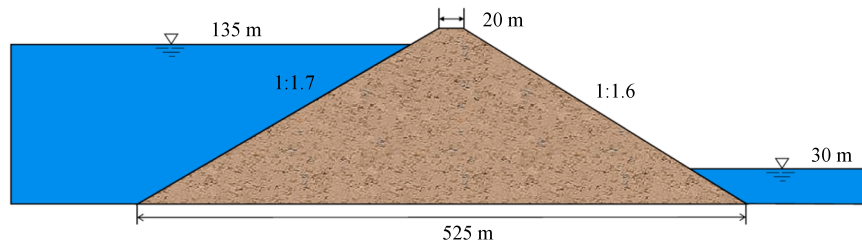


Fig. 12. Geometric model of a homogeneous earth dam.

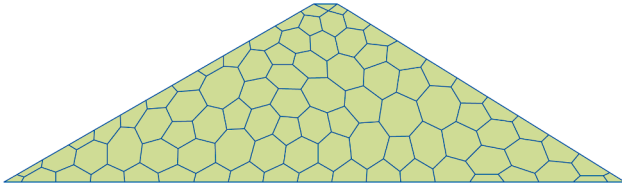


Fig. 13. Computational model of SBFEM with 87 cells and 175 nodes.

insufficient density of the initial mesh, where the location of the water level overflow point was not captured correctly. As the grid is refined, the above errors gradually decreased and the dip line locations generally shows a gradual decrease.

Table 3 presents information on the change in gradient near the infiltration and spillage points during the adaptive process. It can be seen that the gradients near the infiltration and spillage points are larger during the initial calculation, and therefore the infiltration line changes faster near these points. In these regions, the gradient decreases as the grid is progressively refined, causing the free water surface position to gradually stabilize.

#### 4.3. Application of complex panels

##### 4.3.1. Geometry and finite element modelling

The final computational example is an adaptive approach to analyze the steady seepage of a concrete panel rockfill dam over a deep cover. The height of the dam is 56.5 m, the slope ratios of the upstream and downstream dams are 1:1.4 and 1:1.67, respectively, and the upstream water level is 172 m. Concrete panels are connected to concrete toe slabs at the base of the dam and on both sides of the bank, with bedding materials, transition materials, and rock stacking areas underneath. The stratigraphy is divided into two types: deep overburden and bedrock, of which the maximum thickness of the deep overburden reaches 92 m.

The geometric region is discretized using a mixed triangular and quadrilateral mesh, generating a total of 835 cells and 875 nodes, as shown in Fig. 18.

##### 4.3.2. Material parameters

The permeability coefficients of the materials are shown in Table 4.

##### 4.3.3. Analysis scheme

In order to further explore the accuracy and efficiency of the adaptive method, the following three scenarios are used for comparative analysis:

- The grid shown in Fig. 18 is adopted for the calculations.
- Applying the adaptive method for calculation, the adaptive criteria based on Eq. (2.38) for dynamically encrypted cells near the free water surface. Here,  $n$  is taken as 40 and  $\varepsilon$  is taken as  $1e-5$ .
- The dense grid is adopted for the calculations when the dip line position converges.

The finite element mesh models corresponding to scenarios (b) and (c) are given in Fig. 19.

##### 4.3.4. Analysis of results for panel dams

The comparative analysis of the location of the infiltration line shown in Fig. 20 indicates that the computational results of the three scenarios are consistent in terms of the overall trend: the fluid first flows tangentially along the panel, and then gradually infiltrates into the dam body and spreads downstream. However, the effects of different grid strategies on the computational accuracy are significant: The simulation results of scheme (a) with fixed coarse grid division show that the infiltration line is located at about 4.5 m above the built-up base surface, which is inconsistent with the actual situation, leading to a significant reduction in the simulation accuracy of the seepage path inside the dam body; whereas, the results of the adaptive grid of scheme (b) and the globally dense grid of scheme (c) are in high agreement with each other, and the difference in the location of the free-water surface is less than

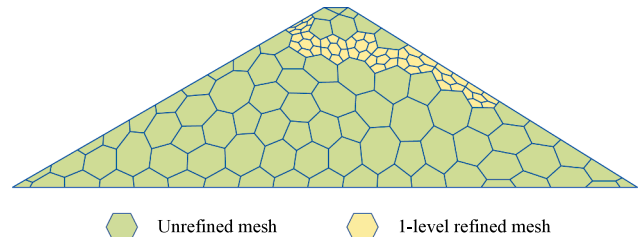


Fig. 15. Schematic of the first refinement of the local grid.

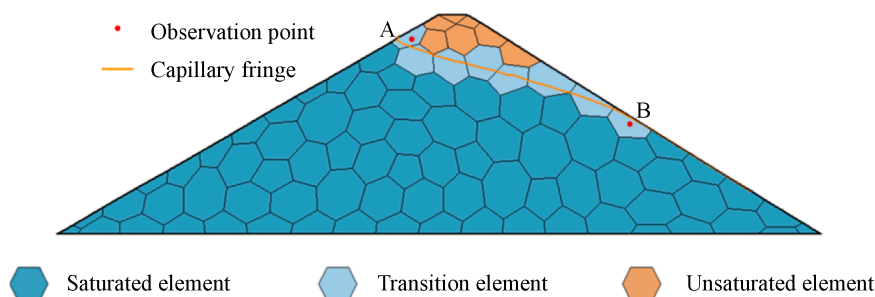


Fig. 14. Definition of different types of elements.



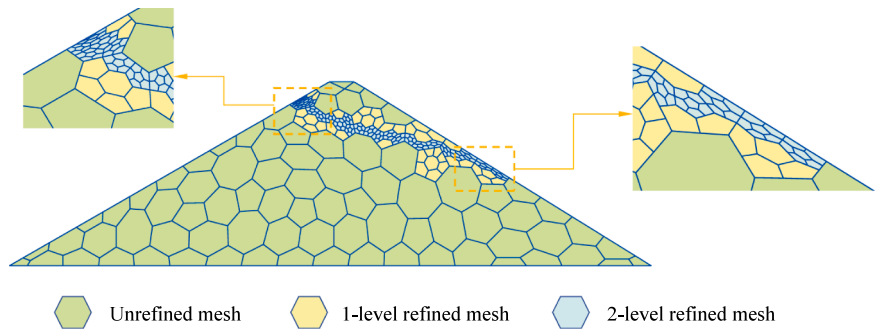


Fig. 16. Adaptive SBFEM computational model.

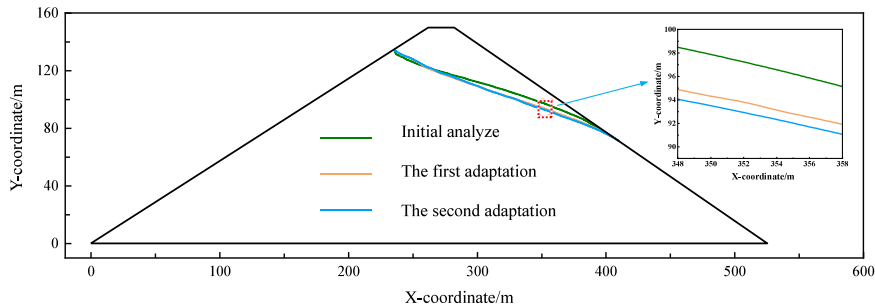


Fig. 17. Adaptive SBFEM computational model.

**Table 3**  
Gradient information at different observation points.

Gradient	X-gradient (Point A)	X-gradient (Point B)	Y-gradient (Point A)	Y-gradient (Point B)
Initial analyze	0.47	0.41	-0.10	-0.19
The first adaptation	0.30	0.36	-0.08	-0.19
The second adaptation	0.25	0.34	-0.07	-0.18

**Table 4**  
The permeability coefficient of main materials.

Materials	Ks(cm/s)	Materials	Ks(cm/s)
Panel	$1 \times 10^{-7}$	Padding zone	$1 \times 10^{-3}$
Toe board	$1 \times 10^{-7}$	Transition zone	$2 \times 10^{-2}$
Impermeable wall	$1 \times 10^{-7}$	Primary rock pile areas	$3 \times 10^{-1}$
Deep cover	$5.5 \times 10^{-3}$	Secondary rock pile areas	$2 \times 10^{-1}$
Bedrock	$1 \times 10^{-5}$		

0.1 %.

The above conclusion can also be verified by the distribution of total head in Fig. 21 : the area of the region with total head below 130 m calculated in scenario (a) is less in size compared to scenario (c) with global refinement of the grid. And the cloud map distribution of total head for scheme (b) is highly consistent with scheme (c).

To further illustrate the accuracy of the adaptive method, the pressure head distributions of the foundations (including bedrock, overburden and impermeable walls) obtained from the calculations of the different analysis methods are given in Fig. 22. Although the pressure head distributions obtained by the three analysis methods have the same

pattern, there is a difference in the values. In order to show this difference, the pressure head distribution at the observation line is analyzed by using the calculation results of scenario (c) as the benchmark solution for this example. Fig. 23 gives the error of pressure head at the observation line for scheme (a) and scheme (b), and it can be seen that the calculation error of scheme (a) is as high as 27 %, which is not able to meet the engineering accuracy, while the calculation error of scheme (b) is less than 0.5 %.

It is worth noting that the computational efficiency of the adaptive analysis is substantially improved, although scenario (b) has the same accuracy as scenario (c). Fig. 24 reveals the core advantage of the

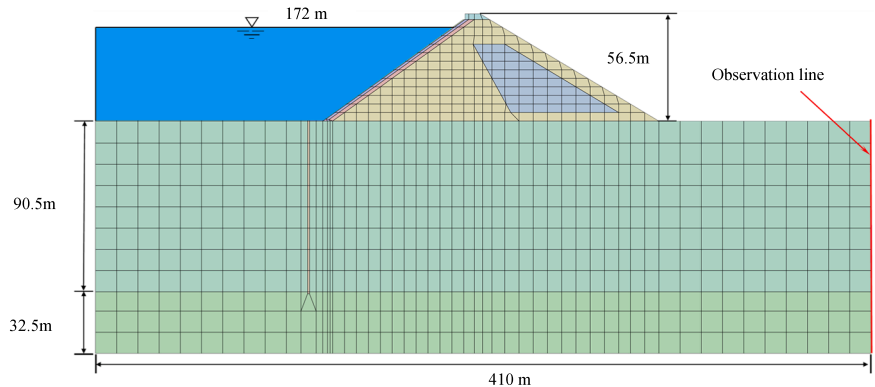
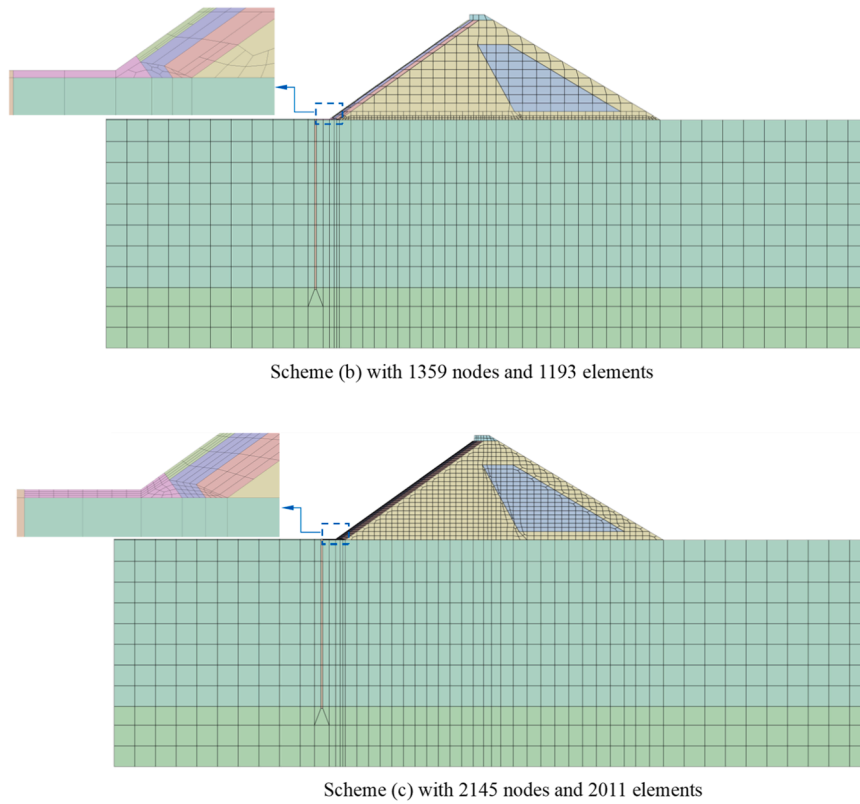
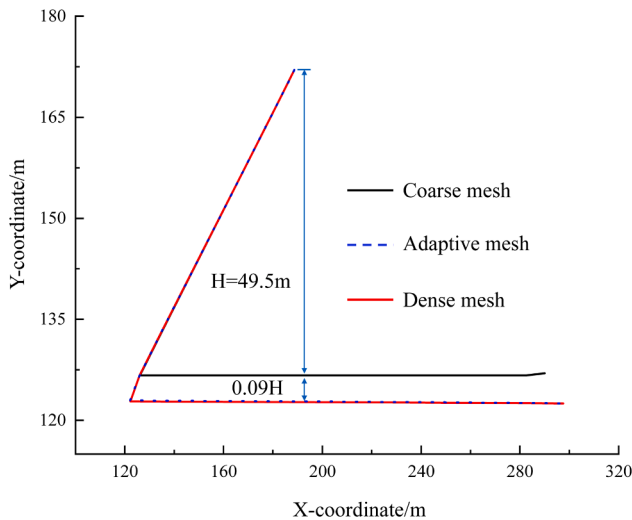


Fig. 18. Computational model of panel dam with 835 cells and 875 nodes.



**Fig. 19.** Finite element models for different analysis scenarios.



**Fig. 20.** Positions of dip lines corresponding to different analysis scenarios.

adaptive approach through a comparative analysis of the computational degrees of freedom, and it can be seen that the computational efficiency of the adaptive analysis is improved by 37 % compared to the global analysis using a fine mesh. In addition, the CPU consumption data in Table 5 (computing platform: Intel Core i7-13700KF @ 4.38 GHz, 16 cores, 15.7GB DDR4 RAM) further validates this advantage, with the adaptive scheme saving 35 % of the computation time compared to traditional dam global refinement.

## 5. Summary

In this study, an adaptive seepage analysis method based on an

improved SBFEM-Polytree coupling framework is proposed, which systematically solves the bottlenecks of grid dependency and computational efficiency in the dynamic simulation of free water surface. The method has been successfully integrated into the self-developed GEO-DYNA finite element platform and systematically verified in the seepage analysis of three types of typical earth and rock dams (vertical earth dams, trapezoidal earth dams and panel rockfill dams), and the main findings are summarized as follows:

- (a) The improved SBFEM-Polytree coupling method proposed in this study shows significant advantages in the seepage analysis of earth-rock dams: firstly, by innovatively arranging the integration points in the domain, combined with the geometrical adaptability of the polytree mesh, it achieves the efficient modelling of the free-water surface problem of earth-rock dams. Secondly, by using the virtual permeability dynamic correction technology, the permeability parameters of the integration points in the domain are adjusted in real time, which ensures the accuracy of the free water surface simulation while avoiding the mesh re-division completely.
- (b) The proposed method can substantially improve the solution efficiency, benefiting from an intelligent free-water surface tracking mechanism and a dynamic grid optimization strategy. Specifically, by developing an adaptive criterion based on a posteriori error estimation, the algorithm is able to automatically identify the key cells traversed by the free water surface after each iteration, thus realizing multi-level subdivision. In the seepage analysis of complex panel dams, by intelligently identifying critical regions and implementing cross-scale grid encryption, this method can achieve the computational accuracy of global refinement by processing only 20 % of the fine grids, while improving the computational efficiency by 37 %.

Based on the existing solution framework, the method can be simply

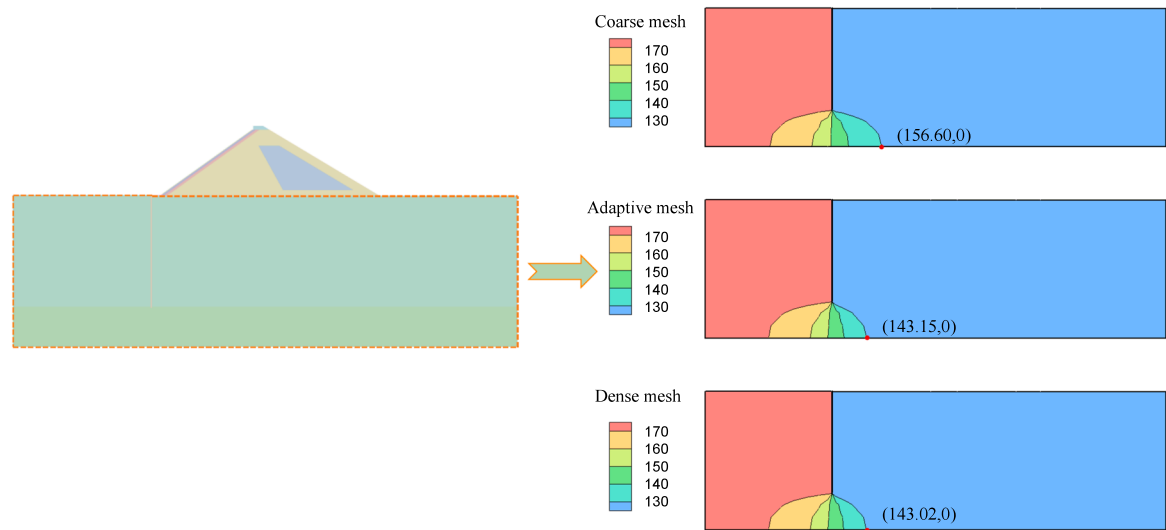


Fig. 21. Total foundation head cloud for different analysis scenarios (units: m).

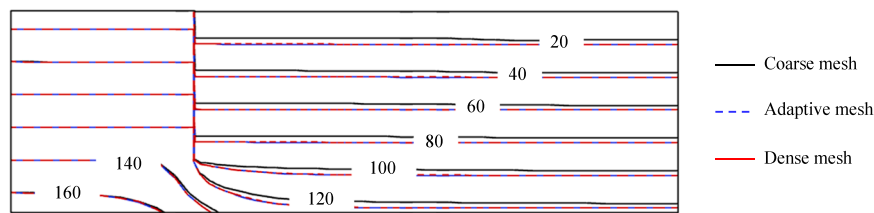


Fig. 22. Foundation pressure head distribution (units: m).

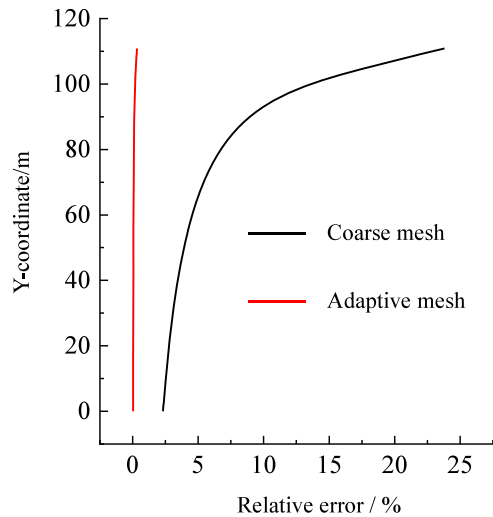


Fig. 23. Relative error in pressure head at observation line (units: %).

extended to 3D infiltration flow analysis, which can provide a high-precision and high-efficiency solution for the simulation of infiltration flow in complex geological environments. It should be noted that the current method is based on steady-state seepage assumptions and does not take into account the effect of the time term for the time being, and is therefore applicable to steady seepage flow conditions. In addition, the method can also take into account the unsaturated characteristics of the soil body, which can provide a new analytical paradigm for the simulation of nonlinear problems, which is also our future research direction.

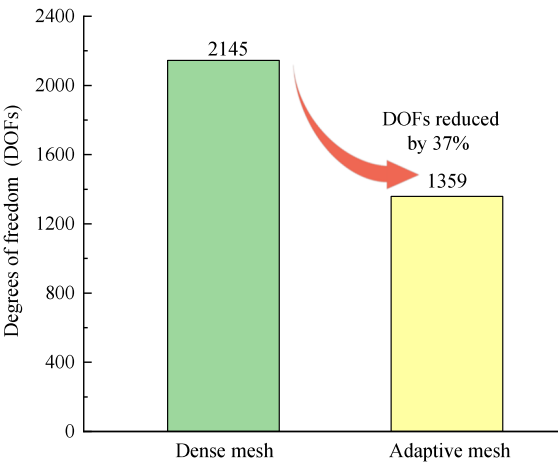


Fig. 24. Comparison of the number of degrees of freedom.

Table 5

CPU consumption statistics for different analysis scheme.

Analysis scheme	Scheme (a)	Scheme (b)	Scheme (c)
CUP Time Consumption (unit: s)	12.11	28.68	44.21

CRediT authorship contribution statement

**Guoyang Yi:** Writing – original draft, Visualization, Validation, Methodology. **Degao Zou:** Writing – review & editing, Supervision, Software, Funding acquisition. **Kai Chen:** Writing – review & editing, Supervision, Resources, Methodology. **Mingliang Zhang:** Visualization,

Methodology, Conceptualization. **Shaoyun Pang**: Validation, Methodology, Investigation.

## Declaration of competing interest

The author declares no conflicts of interest regarding this article.

## Acknowledgements

This work was supported by the National Natural Science Foundation of China (Grant Nos.52192674, 52350393).

## Data availability

Data will be made available on request.

## References

- [1] Di Q, Li P, Zhang M, Guo C, Wang F, Wu J. Three-dimensional theoretical analysis of seepage field in front of shield tunnel face. *Undergr Space* 2022;7(4):528–42. <https://doi.org/10.1016/j.undsp.2021.11.006>.
- [2] Jiang C, Han H, Xie H, Liu J, Chen Z, Chen H. Karst aquifer water inflow into tunnels: an analytical solution. *Geofluids* 2021;2021:1–10. <https://doi.org/10.1155/2021/6672878>.
- [3] Zhang M, Yao D, Lu H, Wang H. Solution of seepage field in different soil layers of concrete dam foundation by flow net method. *IOP Conf Series: Earth Environ Sci* 2020;546(5):52053. <https://doi.org/10.1088/1755-1315/546/5/052053>.
- [4] Su X, Zhang M, Zou D, Zhao Y, Zhang J, Su H. Numerical scheme for solving the richard's equation based on finite volume model with unstructured mesh and implicit dual-time stepping. *Comput Geotech* 2022;147:104768. <https://doi.org/10.1016/j.compgeo.2022.104768>.
- [5] Zhang M, Su X, Zou D, Zhao Y, Zhang J, Su H. A new matrix-free implicit iteration algorithm based on finite volume method for simulating groundwater seepage flows. *Multidiscip Model Mater Struct* 2025. <https://doi.org/10.1108/MMMS-09-2024-0284>.
- [6] Manzini G, Ferraris S. Mass-conservative finite volume methods on 2-d unstructured grids for the richards' equation. *Adv Water Resour* 2004;27(12):1199–215. <https://doi.org/10.1016/j.advwatres.2004.08.008>.
- [7] Lu S, QIAO Y, LIU G. Numerical simulation for one-dimensional unsaturated soil solute transport. *Res Soil and Water Conserv* 2008;15(4):33–6.
- [8] Lima Vivancos V, Voller VR. Two numerical methods for modeling variably saturated flow in layered media. *Vadose Zone J* 2004;3(3):1031–7. <https://doi.org/10.2136/vzj2004.1031>.
- [9] Chávez-Negrete C, Domínguez-Mota FJ, Santana-Quinteros D. Numerical solution of richards' equation of water flow by generalized finite differences. *Comput Geotech* 2018;101:168–75. <https://doi.org/10.1016/j.compgeo.2018.05.003>.
- [10] Lan M, Hu HC, Tian FQ, Hu HP. A two-dimensional numerical model coupled with multiple hillslope hydrodynamic processes and its application to subsurface flow simulation. *Sci China Technol Sci* 2013;56(10):2491–500. <https://doi.org/10.1007/s11431-013-5347-6>.
- [11] Juncu G, Nicola A, Popa C. Nonlinear multigrid methods for numerical solution of the variably saturated flow equation in two space dimensions. *Transp Porous Media* 2012;91(1):35–47. <https://doi.org/10.1007/s11242-011-9831-9>.
- [12] Mingchao L, Xinyu G, Shi J, Zebiao Z. Seepage and stress analysis of anti-seepage structures constructed with different concrete materials in an RCC gravity dam. *Water Sci Eng* 2015;8(4):326–34. <https://doi.org/10.1016/j.wse.2015.10.001>.
- [13] Tian DF, Zheng H, Liu DF. A 2d integrated fem model for surface water-groundwater flow of slopes under rainfall condition. *Landslides* 2017;14(2):577–93. <https://doi.org/10.1007/s10346-016-0716-4>.
- [14] Lazarovitch N, Simunek J, Shani U. System-dependent boundary condition for water flow from subsurface source. *Soil Sci Soc Am J* 2005;69(1):46–50. <https://doi.org/10.2136/sssaj2005.0046>.
- [15] Dai Q, Lei Y, Zhang B, Feng D, Wang X, Yin X. A practical adaptive moving-mesh algorithm for solving unconfined seepage problem with Galerkin finite element method. *Sci Rep* 2019;9(1):6988.
- [16] Jiang S, Du C, Hong Y. Failure analysis of a cracked concrete gravity dam under earthquake. *Eng Fail Anal* 2013;33:265–80. <https://doi.org/10.1016/j.engfailanal.2013.05.024>.
- [17] Chen D, Yang Z, Wang M, Xie J. Seismic performance and failure modes of the jin'anqiao concrete gravity dam based on incremental dynamic analysis. *Eng Fail Anal* 2019;100:227–44. <https://doi.org/10.1016/j.engfailanal.2019.02.018>.
- [18] Xu Z, Yang Y, Cao C. Simulation and analysis of dam leakage inlet detection based on pseudo-flow field method. *J Appl Geophys* 2024;228:105444. <https://doi.org/10.1016/j.jappgeo.2024.105444>.
- [19] Wang H, Ma H, Wu Y, Zhan Z, Xu W, Zhang H, Sun W. Probabilistic analysis of impulse waves generated by large deposits in mountain reservoirs. *Phys Fluids* (1994) 2025;37(4):46615. <https://doi.org/10.1063/5.0266636>.
- [20] Chen Y, Zeng J, Shi H, Wang Y, Hu R, Yang Z, Zhou C. Variation in hydraulic conductivity of fractured rocks at a dam foundation during operation. *J Rock Mech Geotech Eng* 2021;13(2):351–67. <https://doi.org/10.1016/j.jrmge.2020.09.008>.
- [21] Wang X, Yang H, He Y. A temporally piecewise adaptive multiscale scaled boundary finite element method to solve two-dimensional heterogeneous viscoelastic problems. *Eng Anal Bound Elem* 2023;155:738–53. <https://doi.org/10.32604/cmes.2024.048199>.
- [22] Xu Wang X, Yang H, Yang Z, He Y. Development of a three-dimensional multiscale octree SBFEM for viscoelastic problems of heterogeneous materials. *Comput Model Eng Sci*. 2024. <https://doi.org/10.1016/j.enganabound.2023.07.006>.
- [23] Song C, Wolf JP. The scaled boundary finite-element method - alias consistent infinitesimal finite-element cell method - for elastodynamics. *Comput Methods Appl Mech Eng* 1997;147(3-4):329–55. [https://doi.org/10.1016/S0045-7825\(97\)00021-2.s](https://doi.org/10.1016/S0045-7825(97)00021-2.s).
- [24] Song CM, Ooi ET, Natarajan S. A review of the scaled boundary finite element method for two-dimensional linear elastic fracture mechanics. *Eng Fract Mech* 2018;187:45–73. <https://doi.org/10.1016/j.engfracmech.2017.10.016>.
- [25] Song CM. Dynamic analysis of unbounded domains by a reduced set of base functions. *Comput Methods Appl Mech Eng* 2006;195(33-36):4075–94. <https://doi.org/10.1016/j.cma.2005.07.011>.
- [26] Song CM, Tin-Loi F, Gao W. Transient dynamic analysis of interface cracks in anisotropic bimaterials by the scaled boundary finite-element method. *Int J Solids Struct* 2010;47(7-8):978–89. <https://doi.org/10.1016/j.ijsolstr.2009.12.015>.
- [27] Song C. The scaled boundary finite element method in structural dynamics. *Int J Numer Methods Eng* 2009;77(8):1139–71. <https://doi.org/10.1002/nme.2454>.
- [28] Zhang G, Zhao M, Du X, Zhang J. Time-domain scaled boundary perfectly matched layer for elastic wave propagation. *Int J Numer Methods Eng* 2023;124(18):3906–34. <https://doi.org/10.1002/nme.7300>.
- [29] Zhang G, Zhao M, Zhang J, Du X. Scaled boundary perfectly matched layer (sbpml): a novel 3d time-domain artificial boundary method for wave problem in general-shaped and heterogeneous infinite domain. *Comput Methods Appl Mech Eng* 2023;403:115738. <https://doi.org/10.1016/j.cma.2022.115738>.
- [30] Zhang GL, Zhao M, Zhang JQ, Du XL. Prismatic-element sbpml coupled with sbfem for 3d infinite transient wave problems. *Comput Methods Appl Mech Eng* 2024;427. <https://doi.org/10.1016/j.cma.2024.117014>.
- [31] Zhang JQ, Zhao M, Eisenträger S, Du XL, Song CM. An asynchronous parallel explicit solver based on scaled boundary finite element method using octree meshes. *Comput Methods Appl Mech Eng* 2022;401. <https://doi.org/10.1016/j.cma.2022.115653>.
- [32] Zhang JQ, Ankai A, Gravenkamp H, Eisenträger S, Song CM. A massively parallel explicit solver for elasto-dynamic problems exploiting octree meshes. *Comput Methods Appl Mech Eng* 2021;380. <https://doi.org/10.1016/j.cma.2021.113811>.
- [33] Ye W, Zhang J, Yang F, Lin G. A new semi-analytical solution of bending, buckling and free vibration of functionally graded plates using scaled boundary finite element method. *Thin-Walled Struct* 2021;163:107776. <https://doi.org/10.1016/j.tws.2021.107776>.
- [34] Ye W, Liu J, Zang Q, Yin Z, Lin G. Buckling analysis of three-dimensional functionally graded sandwich plates using two-dimensional scaled boundary finite element method. *Mech Adv Mater Struct* 2022;29(17):2468–83. <https://doi.org/10.1080/15376494.2020.1866125>.
- [35] Zhang P, Du C, Birk C, Zhao W. A scaled boundary finite element method for modelling wing crack propagation problems. *Eng Fract Mech* 2019;216:106466. <https://doi.org/10.1016/j.engfracmech.2019.04.040>.
- [36] Zhang P, Du C, Zhao W, Sun L. Dynamic crack face contact and propagation simulation based on the scaled boundary finite element method. *Comput Methods Appl Mech Eng* 2021;385:114044. <https://doi.org/10.1016/j.cma.2021.114044>.
- [37] Du CB, Huang WC, Ghaemian M, Jiang SY, Zhao ZW. New nonlocal multiscale damage model for modelling damage and cracking in quasi-brittle materials. *Eng Fract Mech* 2023;277. <https://doi.org/10.1016/j.engfracmech.2022.108927>.
- [38] Ooi ET, Song C, Natarajan S. A scaled boundary finite element formulation with bubble functions for elasto-static analyses of functionally graded materials. *Comput Mech* 2017;60(6):943–67. <https://doi.org/10.1007/s00466-017-1443-y>.
- [39] Ooi ET, Natarajan S, Song C, Tin-Loi F. Crack propagation modelling in functionally graded materials using scaled boundary polygons. *Int J Fract* 2015;192(1):87–105. <https://doi.org/10.1007/s10704-015-9987-3>.
- [40] Pramod ALN, Ooi ET, Song C, Natarajan S. Numerical estimation of stress intensity factors in cracked functionally graded piezoelectric materials – a scaled boundary finite element approach. *Compos Struct* 2018;206:301–12. <https://doi.org/10.1016/j.compstruct.2018.08.006>.
- [41] Chen K, Zou D, Kong X, et al. An efficient nonlinear octree SBFEM and its application to complicated geotechnical structures. *Comput Geotech* 2018;96:226–45. <https://doi.org/10.1016/j.compgeo.2017.10.021>.
- [42] Chen K, Zou DG, Kong XJ, Chan A, Hu ZQ. A novel nonlinear solution for the polygon scaled boundary finite element method and its application to geotechnical structures. *Comput Geotech* 2017;82:201–10. <https://doi.org/10.1016/j.compgeo.2016.09.013>.
- [43] Chen K, Zou DG, Liu JM, Zhuo Y. A high-precision formula for mixed-order polygon elements based on sbfem. *Comput Geotech* 2023;155. <https://doi.org/10.1016/j.compgeo.2022.105209>.
- [44] Chen K, Zou DG, Yi GY, Nie XP, Qu YQ. A flexible mixed-order formula for tetrahedron elements based on sbfem. *Comput Geotech* 2024;171. <https://doi.org/10.1016/j.compgeo.2024.106390>.
- [45] Zhuo Y, Zou D, Chen K, Qu Y, Yi G, Tian S. Improved double-phase-field algorithm based on scaled boundary finite element method for rock-like materials. *Theor Appl Fract Mech* 2025;138:104916. <https://doi.org/10.1016/j.tafmec.2025.104916>.
- [46] Zou DG, Teng XW, Chen K, Yu X. An extended polygon scaled boundary finite element method for the nonlinear dynamic analysis of saturated soil. *Eng Anal*

- Bound Elem 2018;91:150–61. <https://doi.org/10.1016/j.enganabound.2018.03.019>.
- [47] Zou DG, Teng XW, Chen K, Liu JM. A polyhedral scaled boundary finite element method for three-dimensional dynamic analysis of saturated porous media. *Eng Anal Bound Elem* 2019;101:343–59. <https://doi.org/10.1016/j.enganabound.2019.01.012>.
- [48] Bazayr MH, Graili A. A practical and efficient numerical scheme for the analysis of steady state unconfined seepage flows. *Int J Numer Anal Methods Geomech* 2012;36(16):1793–812. <https://doi.org/10.1002/nag.1075>.
- [49] Bazayr MH, Talebi A. Transient seepage analysis in zoned anisotropic soils based on the scaled boundary finite-element method. *Int J Numer Anal Methods Geomech* 2015;39(1):1–22. <https://doi.org/10.1002/nag.2291>.
- [50] Liu J, Li JB, Li P, Lin G, Xu TJ, Chen LF. New application of the isogeometric boundary representations methodology with sbfem to seepage problems in complex domains. *Comput Fluids* 2018;174:241–55. <https://doi.org/10.1016/j.compfluid.2018.08.004>.
- [51] Yang Y, Zhang ZL, Yi Feng, Wang K. A novel solution for seepage problems implemented in the Abaqus UEL based on the polygonal scaled boundary finite element method. *Geofluids* 2022. <https://doi.org/10.1155/2022/5797014>. 2022.
- [52] Yan MJ, Yang Y, Zhang ZL, Su C, Luo TF. A psbfem approach for solving seepage problems based on the pixel quadtree mesh. *Geofluids* 2023. <https://doi.org/10.1155/2023/9092488>. 2023.
- [53] Johari A, Heydari A. Reliability analysis of seepage using an applicable procedure based on stochastic scaled boundary finite element method. *Eng Anal Bound Elem* 2018;94:44–59. <https://doi.org/10.1016/j.enganabound.2018.05.015>.
- [54] Hajiazizi M, Graili A. Efficient scaled-boundary radial point interpolation method for unsteady confined-seepage flow through nonhomogeneous and anisotropic soils. *Int J Geomech* 2018;18(6). [https://doi.org/10.1061/\(ASCE\)GM.1943-5622.0001143](https://doi.org/10.1061/(ASCE)GM.1943-5622.0001143).
- [55] Bathe KJ, Khoshgoftaar MR. Finite-element free-surface seepage analysis without mesh iteration. *Int J Numer Anal Methods Geomech* 1979;3(1):13–22. <https://doi.org/10.1002/nag.1610030103>.